



Electron-hole interactions in choline-phosphotungstic acid boosting molecular oxygen activation for fuel desulfurization

Xingye Zeng^{a,b}, Xinyan Xiao^{a,*}, Jiayi Chen^a, Hanlu Wang^b

^a School of Chemistry and Chemical Engineering, Guangdong Provincial Key Lab of Green Chemical Product Technology, South China University of Technology, Guangzhou 510640, PR China

^b College of Chemical Engineering, Guangdong University of Petrochemical Technology, Maoming, 525000, PR China

ARTICLE INFO

Keywords:

Phosphotungstic acid
Electron-hole interactions
Molecular oxygen
Fuel desulfurization
Straight-run gasoline

ABSTRACT

Many studies have been conducted regarding the separation behavior of carriers (electrons and holes) because of involving the generation of superoxide radicals ($O_2^{\cdot-}$), hydroxyl radicals (HO^{\cdot}), and hydrogen peroxide (H_2O_2) in the photocatalytic process of heteropolyacids. Instead, relatively little attention has been focused on the potential Coulomb interactions between photogenerated electrons (e^-) and holes (h^+). Herein, choline-phosphotungstic acid (Ch_3 -HPW) was synthesized via one-step acid-base neutralization reaction method, and characterized. The electronic excited state analysis of Ch_3 -HPW showed that the formation of singlet oxygen (1O_2) was related to the electron-hole interactions in the photocatalytic process of ground state molecular oxygen (3O_2) activation. Subsequently, a facile fuel photocatalytic oxidative desulfurization and extraction system was established on the basis of Ch_3 -HPW, air, and acetonitrile (MeCN), to better understand the 3O_2 activation in specific applications. The main photocatalytic reaction conditions affecting the desulfurization process, including the amount of Ch_3 -HPW, the volume ratio of MeCN to model oil, the initial S-concentration, air/ N_2 bubbling, sulfur compounds, and fuel composition, were systematically investigated under UV radiation. The sulfur removal for model oil and straight-run gasoline in the system were 99.6% and 89.9%, respectively. The results of radical scavenger experiments, electron spin-resonance (ESR) spectroscopy, and density functional theory (DFT) calculations further demonstrated that 1O_2 , H_2O_2 , and h^+ played important roles in the oxidation of sulfur-containing compounds. A new method was developed for the desulfurization of liquid fuels using green and inexpensive O_2 in this work to promote the development of photocatalytic process of exciton-involved HPA-based photocatalysts.

1. Introduction

The removal of sulfur compounds from liquid fuels has become an urgent task in recent years because of the strict environmental regulations and the development of fuel cell applications. Sulfur content needs to be reduced to below 1 part per million (ppm) by weight to avoid poisoning reforming catalysts, water-gas-shift catalysts, and the electrodes in fuel cell systems [1]. Hydrodesulfurization (HDS) is a predominant technology for the removal of sulfur compounds from liquid fuels. This process involves high temperature ($\sim 400^\circ C$), high hydrogen pressure (150–2250 psi), precious metal catalysts, and large reactors [2,3]. However, heterocyclic aromatic sulfur compounds (HASCs), especially dibenzothiophene (DBT) and alkyl substituted DBTs, are difficult to remove using the HDS process unless energy-intensive and capital-intensive processes are used [4]. To reduce the energy and

hydrogen consumption for desulfurization, increasing attentions have been paid to non-HDS methods, such as reductive desulfurization [5], extractive desulfurization [6], adsorptive desulfurization [7], oxidative desulfurization (ODS) [8], photocatalytic desulfurization (PDS) [9], and their combination technologies [10]. Among the developing desulfurization methods, the PDS method has shown great promise because of its unique advantages, such as activation of chemical reaction by photon instead of temperature, carbon neutral, and the use of abundant and virtually permanent solar energy [11].

Many effective PDS systems have been developed with various semiconductor-based photocatalysts, such as TiO_2 [12], SiO_2 - TiO_2 [13], Cu - Fe / TiO_2 [14], CeO_2 / TiO_2 [15], CeO_2 /attapulgite/ g - C_3N_4 [16], Pt - RuO_2 / TiO_2 [17], Pt - RuO_2 / $BiVO_4$ [18], and RuO_2 / SO_4^{2-} - TiO_2 [19]. Most efforts are aimed at examining different photocatalysts and improving desulfurization efficiency. According to the widely accepted

* Corresponding author.

E-mail address: cexyxiao@scut.edu.cn (X. Xiao).

<https://doi.org/10.1016/j.apcatb.2018.09.038>

Received 15 July 2018; Received in revised form 6 September 2018; Accepted 11 September 2018

Available online 12 September 2018

0926-3373/ © 2018 Elsevier B.V. All rights reserved.

semiconductor band structure theory, the separation and migration of photogenerated charge carriers are the key factors affecting photocatalytic activity. Hence, it is a popular strategy to improve desulfurization performance by utilizing charge-separation efficiency methods, such as transition metal ion doping, noble metals deposition, the construction of semiconductor heterojunctions [13–19]. As an environmentally friendly and mature industrial catalyst, heteropolyacid (HPA) has long been ignored by PDS. This is because HPAs is short of a canonical energy-band structure compared with a semiconductor. The essence of photogenerated carriers in a HPA is the charge transfer from an oxygen atom to the *d* orbitals of metal atom in the presence of light with abundant energy. For instance, the excitation of phosphotungstic acid (HPW) refers to the charge transfer from O^{2-} to W^{6+} , leading to the formation of a hole center ($O^{\cdot-}$) and trapped electron center (W^{5+}) pair [20]. Compared with the electrons in the conduction band and the holes in the valence band in a semiconductor, the further separation and free migration between the holes and electrons are mutually restricted in a HPA under irradiation. This restriction is mainly caused by non-negligible Coulomb interactions between the holes and the electrons in a HPA. Consequently, HPAs are not ideal candidates for PDS at the view of charge carriers.

Recent researches show that traditional strategies for charge-carrier regulation including band structure design and charge separation optimization are deemed to be effective for achieving advanced photocatalytic processes, which are somehow incomplete once the excitonic effects are taken into account [21–23]. Xie et al. have brightened that the spatial-confinement-induced excitonic effects play crucial roles in photocatalytic processes of heterolayered inorganic semiconductors for molecular oxygen (O_2) activation [21]. These reports not only provide a strategy for activating O_2 , but also imply that the excitonic effect plays an important role in photocatalytic activity. The inspiring results encourage us to interrogate the influence of excitonic effects toward the potential Coulomb interactions in the photocatalytic process of HPA-based photocatalysts.

Generally, pure HPAs in presence of extractant in desulfurization systems, suffer from the difficulties in separation and recovery of catalysts after the reactions since they are very soluble in polar solvents [24]. Consequently, after reacting with quaternary ammonium or quaternary ammonium salt (QAS), HPA was modified into a QAS-HPA-type catalyst in the previous ODS systems, such as $[C_{18}H_{37}N(CH_3)_3]_4[H_2NaPW_{10}O_{36}]$ [25], $[(CH_3)_3NC_{16}H_{33}]_4W_{10}O_{32}$ [26], and $[(C_{18}H_{37})_2N(CH_3)_2]_5IMo_6O_{24}$ [27]. Although QAS-HPA with long carbon chains has better surface activity, the long carbon chains exhibit “soft” characteristics that may result in localizing the charge carriers due to polaronic relaxation [28]. Meanwhile, QAS-HPA with long carbon chains is strongly lipophilic, resulting in the formation of metastable droplets that require additional demulsification to separate the catalyst [29].

In this work, we focus on QAS-HPA with short carbon chains, which keeps the rigid lattice structures and appropriate surface activity. Firstly, taking choline-phosphotungstic acid (Ch_3 -HPW) as an example, the excitonic effect existing in Ch_3 -HPW may greatly affect the photocatalytic O_2 activation behaviors and the results were examined through experiments and calculations. Then, a simple extraction and photocatalytic oxidation desulfurization (EPODS) system consisting of the catalysts Ch_3 -HPW, air, and acetonitrile (MeCN) was established to evaluate its effectiveness in removing sulfur compounds sulfur compounds in model oil and real oil, respectively. Finally, a probable reaction mechanism was proposed based on the radical scavenger experiments, electron spin-resonance (ESR) spectroscopy, and density functional theory (DFT) calculations.

2. Experimental and computational methods

2.1. Materials

Benzothiophene (BT, 97%), DBT (98%), 4-methyldibenzothiophene (4-MDBT, 97%), 4,6-dimethyldibenzothiophene (4,6-DMDBT, 98%), *n*-decane (AR), tetradecane (AR), and phosphotungstic acid hydrate (HPW, $H_3PW_{12}O_{40} \cdot xH_2O$, reagent grade) were purchased from Aladdin Industrial Corporation. Choline (Ch) solution 48–50 wt% in water was obtained from Energy Chemical Technology (Shanghai) Co., Ltd. Straight-run gasoline (SRG) was obtained from Maoming petrochemical company and stored in a refrigerator below 8 °C before use. Other chemical reagents were purchased from Tianjin Kermel Chemical Reagent Co., Ltd (China). All chemicals were analytical reagent grade and used without further purification.

2.2. Preparation of Ch_3 -HPW sample

Ch_3 -HPW was synthesized via one-step acid-base neutralization reactions without any byproducts except water. Firstly, 3.6 g of HPW and 0.93 g of Ch solution were dissolved in 40 mL and 20 mL of deionized water, respectively. Under ultrasonication, the diluted solution of Ch was slowly dropped into the HPW solution to immediately generate a white precipitate. The mixed solution was stirred for 5 h and dry overnight at 80 °C to remove water. The white product was further washed three times with deionized water and dry at 80 °C for 5 h.

2.3. Characterizations

The Fourier transform infrared (FT-IR) spectra of the samples, diluted with KBr and pressed into a pellet, were recorded on a Thermo-Nicolet Nexus 670 FT-IR spectrometer. The ultraviolet-visible (UV-vis) spectra were collected on a Hitachi UV-3010 spectrophotometer (BaSO₄ as a reflectance standard). The steady-state and time-resolved photoluminescence (PL) spectra were acquired on an FLS980 fluorescence spectrometer (Edinburgh Instruments Ltd). The contents of C, H, and N of Ch_3 -HPW were determined by vario EL cube elemental analyzer. Thermo-gravimetric and differential scanning (TG-DSC) analysis were performed on Netzsch STA-449F3 Jupiter. The content of tungsten was measured by gravimetric determination in muffle burning at 850 °C for 40 min. X-ray fluorescence (XRF) was performed with a Rigaku Supermini 200 spectrometer to determine the P/W molar ratios. The contact angle measurements were performed using a pellet of the samples and subsequently adding a drop of 4 μ L of water on the surface of samples. The pictures obtained from the water drop on the surface of samples were used to get the contact angle formed between the water and the samples.

The X-ray diffraction (XRD) patterns were collected on a Rigaku Ultima IV diffractometer with Cu K α radiation ($\lambda = 1.54178$ Å). The scanning electron microscopy (SEM) images and energy dispersive X-ray spectroscopy (EDX) maps were acquired on a Hitachi SU8220 field emission scanning electron microscope. The transmission electron microscope (TEM) measurements were conducted on a FEI Tecnai G2 F20 TEM operating at 200 kV. X-ray photoelectron spectroscopy (XPS) measurements were performed using a multifunctional imaging electron spectrometer (Thermo Escalab 250Xi) with Al K α radiation. The X-band ESR spectra were recorded at ambient temperature on a JEOL JES FA200 spectrometer.

2.4. Desulfurization testing

The model oil was prepared by dissolving BT, or DBT, or 4-MDBT, or 4,6-DMDBT in *n*-decane with a corresponding S-concentration of 500 ppm. Desulfurization of the model oil was carried out in a home-made batch photocatalytic reactor equipped with a high pressure mercury lamp (100 W, main wave length 365 nm, 0.2 mW/cm²), as

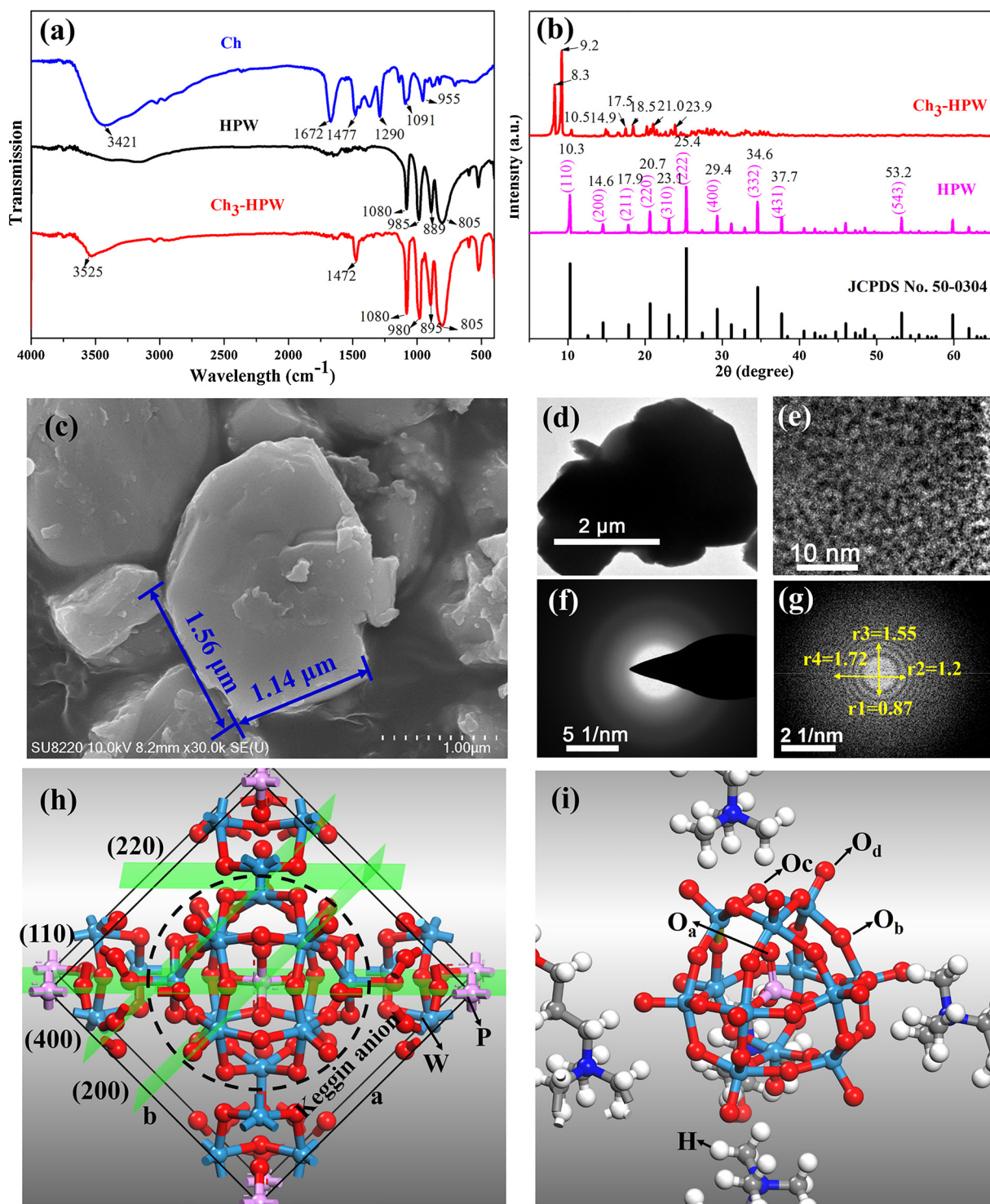


Fig. 1. Structural Characterization. (a) FT-IR spectra of HPW and Ch₃-HPW; (b) XRD patterns of HPW and Ch₃-HPW; (c) FESEM image of Ch₃-HPW; (d) TEM image, (e) HRTEM image, the corresponding (f) SAED pattern and (g) FFT SAED pattern of Ch₃-HPW; (h) Schematic structural view of HPW; (i) Speculated structure of Ch₃-HPW.

shown in Fig. S1 in the Supporting information (SI). According to the specific reaction conditions, 15 mL of model oil, a certain amount of catalysts, MeCN, and air were mixed in the quartz reactor with magnetic stirring. 50 μ L of the oil samples were periodically removed and further analyzed using gas chromatography flame ionization detection on Agilent GC-7820 A (HP-5 column, l 30 m \times Φ 0.32 mm \times 0.25 μ m) by adding tetradecane as an internal standard. The chromatographic procedure were as follows: injection volume of 0.2 μ L, inlet temperature

of 250 $^{\circ}$ C, detector temperature of 270 $^{\circ}$ C, column temperature of 140 $^{\circ}$ C heated to 170 $^{\circ}$ C (with 10 $^{\circ}$ C min $^{-1}$ increases), holding at 170 $^{\circ}$ C for 1 min then heating to 230 $^{\circ}$ C (with 15 $^{\circ}$ C min $^{-1}$ increases), and holding at 230 $^{\circ}$ C for 3 min. According to the analysis by GC (Fig. S2), the residual S-containing products in the oil phase were not observed after the desulfurization reaction. The conversion of BT, DBT, 4-MDBT, or 4,6-DMDBT in model oil was used to indicate the sulfur removal percentage, which was calculated by the following Eq. (1):

$$\text{Sulfur removal percentage} = (C_0 - C_t)/C_0 \times 100\% \quad (1)$$

where C_0 was the initial sulfur content and C_t was the sulfur content of the model oil after catalytic at time t . After reaction, the MeCN phase was separated and diluted 10 times with methanol to study the photocatalytic oxidizing products using gas chromatography-mass spectrometry (GC–MS) on Shimadzu GC–MS QP2010 plus.

Straight-run gasoline (SRG) was chosen as a real oil example for desulfurization testing. The sulfur content of SRG was determined by combustion/ultraviolet fluorescence method on Thermo Scientific iPRO 5000 series. The contents of paraffins, olefins, naphthenes, and aromatic (PONA) in SRG were determined by gas chromatography on Agilent GC-7890B (HP-PONA column, l 50 m \times ϕ 0.2 mm \times 0.5 μ m) with the known hydrocarbon composition database obtained from Sinopec research institute of petroleum processing.

2.5. Computational details

DFT and time-dependent DFT (TD-DFT) calculations [30] were carried out for $\text{Ch}_3\text{-HPW}$ and HPW by using the B3LYP [31] functional and an mixed basis (lanl2dz for W atom and 6–31 g(d, p) for P, C, N, O, and H atoms) in vacuum. The excited energies for HASC and the molecular orbital energies for DBT and reactive oxygen species (ROS) were calculated using B3LYP/6-311 + g(d, p), and solvent effects in MeCN were considered using the polarizable continuum model (PCM) [32]. All DFT calculations were completed in the Gaussian 09 software package [33] and electron excitation analysis were performed with the help of the program Multiwfn [34].

The Coulomb attractive energy (E_c) between electron and hole, which can be calculated as simple Coulomb formula (2) in Multiwfn:

$$E_c = - \int \int \frac{\rho_h(\vec{r}_1)\rho_e(\vec{r}_2)}{|\vec{r}_1 - \vec{r}_2|} d\vec{r}_1 d\vec{r}_2 \quad (2)$$

where ρ represents the electronic densities of the hole ρ_h and the particle (electron) ρ_e with their coordinates \vec{r}_1 and \vec{r}_2 , respectively. The exciton binding energy (E_b) is given by [35]

$$E_b = - \frac{e^2}{4\pi\epsilon_0\epsilon_r} E_c \quad (3)$$

where e is the elementary charge, ϵ_0 is the vacuum permittivity, and ϵ_r is relative dielectric constant given by

$$\frac{\epsilon_r - 1}{\epsilon_r + 2} = \frac{4\pi}{3} \frac{1}{V_M} \alpha' \quad (4)$$

Here, V_M and α' are the molecular volume and the polarizability volume, respectively, which can be calculated by DFT method.

3. Results and discussion

3.1. Structural characterizations

As shown in Fig. 1a, the characteristic absorption bands for the HPW Keggin anion in the FT-IR spectrum of $\text{Ch}_3\text{-HPW}$ were observed at 1080, 980, 895, and 805 cm^{-1} , corresponding to the asymmetric vibrations of central oxygen (P–O_a), terminal asymmetric oxygen (W–O_d), corner shared oxygen (W–O_b–W), and edge shared oxygen (W–O_c–W), respectively [36]. This indicated that the structure of the Keggin anion is well retained after the organic cation replaced the proton in HPW. The absorption bands at 3525 and 1472 cm^{-1} were attributed to C–OH stretching vibration of primary alcohols and C–H asymmetric bending, suggesting the existence of the Ch group [37]. Compared with pure Ch (3421 cm^{-1}), the absorption feature of the C–OH stretching vibration in $\text{Ch}_3\text{-HPW}$ had the higher band location (3525 cm^{-1}), weakened and narrowed adsorption band. This indicated the intramolecular H–bonds were dramatically weakened in $\text{Ch}_3\text{-HPW}$ after the proton of HPW reacted with –OH of Ch.

Elemental analysis (EA), X-ray fluorescence (XRF), energy-dispersive X-ray spectroscopy (EDX), and TG-DSC were further performed to understand the content of each element in $\text{Ch}_3\text{-HPW}$, given in Table S1 and Fig. S3 (SI) in details. The normalization values of C, H, N, O, P, and W-contents were 5.16%, 1.52%, 1.21%, 22.57%, 0.98%, and 68.57%, respectively, and the corresponding calculated values were 5.59%, 1.44%, 1.30%, 22.32%, 0.96%, and 68.39%, respectively. According to these results, it was presumed that the molecular formula of $\text{Ch}_3\text{-HPW}$ is $[\text{HOC}_2\text{H}_5\text{N}(\text{CH}_3)_3]_3[\text{PW}_{12}\text{O}_{40}] \cdot 0.5\text{H}_2\text{O}$.

The XRD patterns were shown in Fig. 1b. There are several intense diffraction peaks observed for HPW: 10.3°(110), 14.6°(200), 17.9°(211), 20.7°(220), 25.4°(222), 29.4°(400), 34.6°(332), 37.7°(431), and 53.2°(543) which are all found within $2\theta = 10\text{--}60^\circ$ [38]. They are fully consistent with characteristic peaks of $\text{H}_3\text{PW}_{12}\text{O}_{40} \cdot 6\text{H}_2\text{O}$ (JCPDS card No. 50-0304) with typical body-centered cubic phase structure. Compared with HPW, the XRD pattern of $\text{Ch}_3\text{-HPW}$ showed two new sharp peaks at 2θ of 8.3° and 9.2° and a relative broad and weak diffraction peaks with $2\theta = 10\text{--}60^\circ$, which indicated its small size and poor crystallinity [39]. Further, the field-emission scanning electron microscopy (FESEM) and TEM images gave direct evidence that the sample size becomes small after HPW reacted with Ch. According to the results of FESEM analysis, the sample size of HPW (Fig. S4 in SI) was estimated to be 20–30 μm and the size of $\text{Ch}_3\text{-HPW}$ (Fig. 1c in FESEM and Fig. 1d in TEM) was estimated to be 1–3 μm . And no obvious lattice fringe can be found in high resolution transmission electron microscopy (HRTEM) image (Fig. 1e) for $\text{Ch}_3\text{-HPW}$, which further confirmed that $\text{Ch}_3\text{-HPW}$ exhibits very poor crystal orientation. The selected-area electron diffraction (SAED) pattern (Fig. 1f) for $\text{Ch}_3\text{-HPW}$ gives multiple broadened diffraction rings. No diffraction ring can be observed in the SAED pattern (Fig. 1f), which is probably due to the high sensitivity of the $\text{Ch}_3\text{-HPW}$ surface for electron beam. Hence, the fast Fourier transform SAED (FFT SAED) image (Fig. 1g) was further obtained from the HRTEM image (Fig. 1e). Just as expected, clear polycrystalline diffraction rings can be expectedly found in FFT SAED image with a radius ratio of 1:2:3:4, which indicated that the sample structure is transformed from the body-centered cubic phase to a simple orthorhombic structure. Consequently, the diffraction peak at 2θ of 8.3° and 10.3° were indexed to the (001) and (110) crystal planes. Generally, the diffraction of (001) plane is hard to observe due to the systematic absence rules in the body-centered cubic phase in pure HPW.

The crystal structure of HPW was shown in Fig. 1h. Based on the above characterization results, the putative structure of $\text{Ch}_3\text{-HPW}$ was that a Keggin anion is surrounded by several Ch_3 cations, as shown in Fig. 1i. Clearly, the high Miller index crystal surface of the $\text{Ch}_3\text{-HPW}$ structure is greatly attenuated relative to the bare HPW, which was in agreement with an analysis of the aforementioned XRD patterns.

To validate the chemical constitution of the as-synthesized $\text{Ch}_3\text{-HPW}$, the sample was further studied by XPS analysis, as shown in Fig. 2. The XPS survey spectrum (Fig. 2a) confirms the presence of C, O, N, P, and W elements, further indicating that HPW have reaction with Ch. As shown in Fig. 2b, the binding energy peak around 36.3 eV is ascribed to W 4f_{7/2}, while the peak around 38.4 eV is assigned to W 4f_{5/2}. The binding energy of 36.3 eV for W 4f_{7/2} core excitation is approximately equal to that of W⁶⁺, confirming that such oxidation state of tungsten could be ascribed to $\text{PW}_{12}\text{O}_{40}^{3-}$ Keggin anions reported elsewhere [40]. Moreover, the lower binding energies at 34.9 and 37.2 eV are corresponded to the oxidation state of W⁵⁺, which may be caused by a small amount of electron transfer from Ch to HPW [41]. The XPS spectrum of O 1s could be fitted by three peaks at binding energies of 531.3, 532.6, and 533.3 eV (Fig. 2c), which are ascribed to the W–O–W, PO₄³⁻, and C–OH, respectively [42]. The high-resolution XPS spectra of other elements, such as C 1s (Fig. 2d), N 1s (Fig. S5a in SI), and P 2p (Fig. S5b in SI), further confirm that the Ch has been successfully introduced to the as-prepared $\text{Ch}_3\text{-HPW}$. The XPS analysis provides further confirmation of the above-mentioned speculated $\text{Ch}_3\text{-HPW}$ structure.

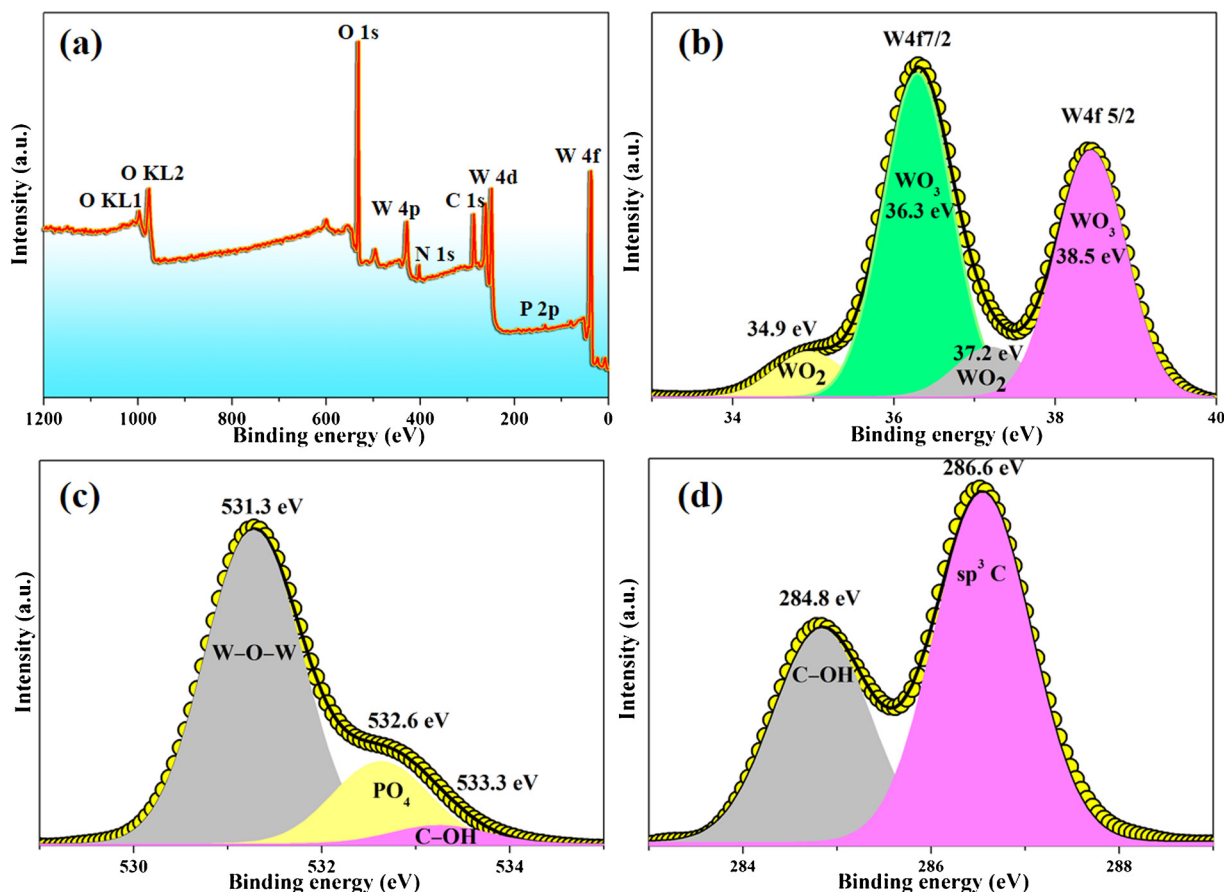


Fig. 2. XPS spectra of $\text{Ch}_3\text{-HPW}$: (a) survey spectrum, and high-resolution XPS spectra of (b) W 4f, (c) O 1s, and (d) C 1 s.

3.2. UV-vis DRS and PL spectroscopic properties

Besides the morphology and crystal structure, it is well known that the optical property of photocatalyst plays an important role in its photocatalytic activity. To further understand the charge carrier generating, trapping, and transfer behaviors, the UV-vis diffuse reflectance spectra (UV-vis DRS), steady-state and time-resolved photoluminescence spectra (PL) were performed. As displayed in Fig. 3a, light absorption of HPW at ~ 248 and ~ 347 nm are assigned to charge transfer from an O_{2p} to W_{5d} orbitals at $\text{W}=\text{O}_d$ and $\text{W}-\text{O}_{b/c}-\text{W}$ bonds, respectively [36]. When HPW is bound to Ch, the absorption peaks at $\text{W}=\text{O}_d$ and $\text{W}-\text{O}_{b/c}-\text{W}$ bonds are observed to blue shift to ~ 237 and ~ 303 nm, respectively. The significant blue shift of 44 nm for the characteristic absorption at $\text{W}-\text{O}_{b/c}-\text{W}$ bond is greater than that of $\text{W}=\text{O}_d$ bond of 11 nm, indicating that the $\text{O}_{b/c}$ atoms in Keggin structure are more easily affected after HPW binding to Ch. Typically, the band gap is attributed to the direct transition for HPW and HPW composites [40,43]. Hence, the estimated band-gap energy (E_g) of HPW and $\text{Ch}_3\text{-HPW}$ were ~ 3.08 and ~ 3.26 eV, respectively, from a plot of $(ah\nu)^2$ versus photon energy ($h\nu$) (Fig. 3b). It is reasonable that interaction of HPW with Ch_3 causes the slightly expansion of E_g for $\text{Ch}_3\text{-HPW}$. According to a straightforward understanding analogous to the energy-band structure of a solid semiconductor, the results tentatively indicate that $\text{Ch}_3\text{-HPW}$ has an enhancing redox ability based on the blue shift of the absorption band and the broadening of the band gap.

As displayed in Fig. 3c, steady-state PL spectra recorded at 25°C exhibit similar emission peaks for HPW and $\text{Ch}_3\text{-HPW}$. $\text{Ch}_3\text{-HPW}$ exhibits the higher intensity of PL spectrum than that of HPW. The rational reason is attributed to the interaction between Ch and HPW, which has been confirmed by aforementioned UV-vis and XPS analysis. Notably, the direct band-gap natures of HPW and $\text{Ch}_3\text{-HPW}$ are

responsible for the clear PL intensities at room temperature. Generally, band-edge emission peaks are usually observed in inorganic semiconductors, mainly resulting from band-edge free excitons (electron-hole pairs) [28,44]. Based on the estimated E_g , the theoretical band-edge emission peaks for HPW and $\text{Ch}_3\text{-HPW}$ should occur at ~ 402 (~ 3.08) and ~ 380 nm (~ 3.26 eV), respectively. Unexpected, no band-edge emission close to the theoretical value were observed, suggesting that the photogenerated free electrons and holes may convert to near-band-edge binding excitons. The dominant emission peaks for HPW and $\text{Ch}_3\text{-HPW}$ were observed at ~ 413 and ~ 412 nm, respectively, indicating that the values of E_b are very close. With respect to the theoretical emission peak, however, the dominant emission peaks for HPW and $\text{Ch}_3\text{-HPW}$ were red-shifted by 10 (0.08) and 32 nm (0.26 eV), respectively. This phenomenon shows that more energy loss in $\text{Ch}_3\text{-HPW}$ occurs during the formation of binding excitons by photogenerated free electrons and holes [43]. The lost energy may be transferred to other molecules around, such as the ground state molecular oxygen ($^3\text{O}_2$). Time-resolved PF spectra were employed to get collective information on the excitation kinetics of the samples. Monoexponential function is employed to fit the tails of the PF decay kinetics, yielding the mean lifetimes of ~ 0.76 and ~ 0.78 ns for HPW and $\text{Ch}_3\text{-HPW}$ (Fig. 3d), respectively. The nanosecond lifetimes indicate the fairly fast irradiative recombination for excitonic recombination in the samples [21]. This also shows that it is quite difficult to further separate the short-lived binding excitons into free electrons and holes [23]. Therefore, it is speculated that it is an important reason for the photocatalytic activity derived from the energy transfer of excitons. Overall, these results demonstrated the non-negligible excitonic effects in the samples, inspiring us to further interrogate the details of electron excitation in the photocatalytic process.

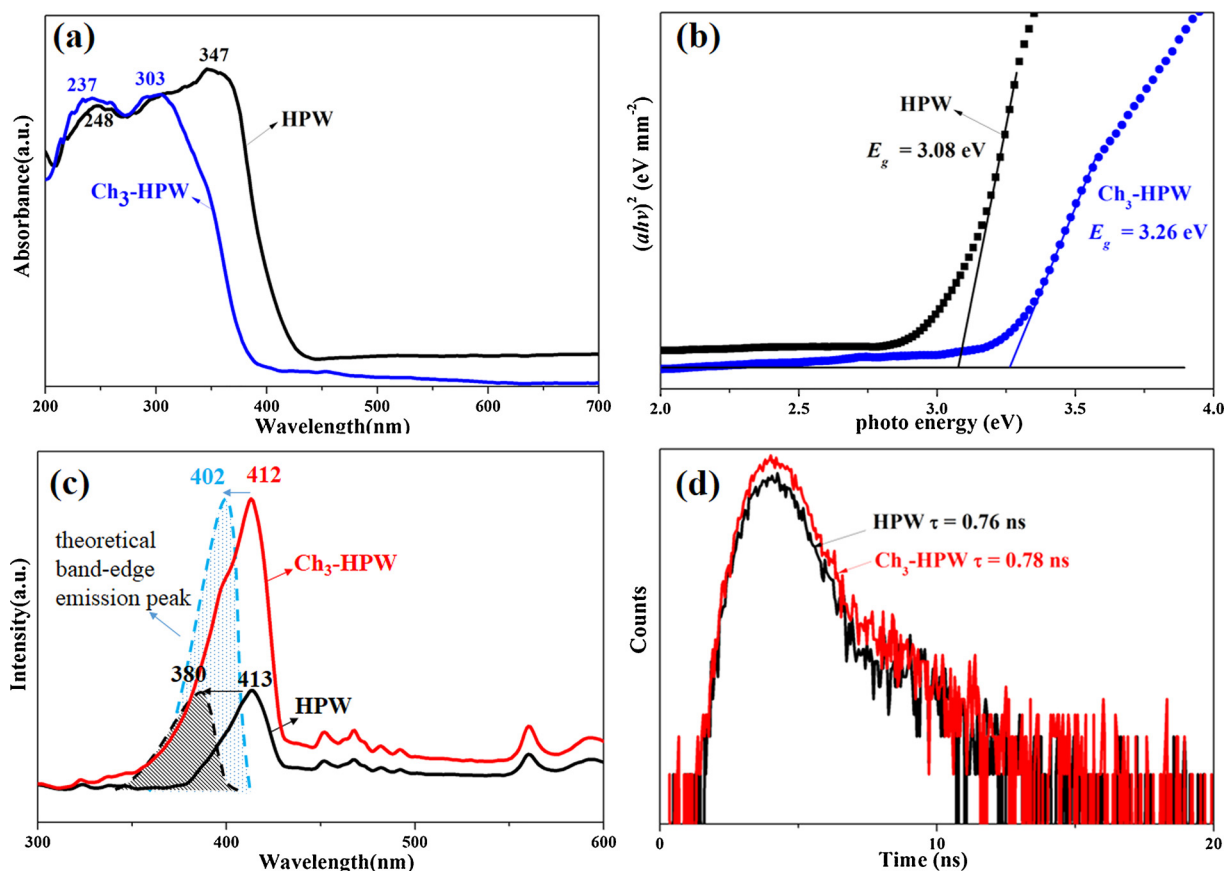


Fig. 3. (a) UV-vis DRS of HPW and Ch₃-HPW. (b) Plots of $(ah\nu)^2$ vs photon energy ($h\nu$) for HPW and Ch₃-HPW. (c) Steady-state PL spectra of HPW and Ch₃-HPW at an excitation wavelength of 260 nm. (d) Time-resolved PL spectra of HPW and Ch₃-HPW, which can be fitted using a multi-exponential function, $I_{PL}(t) = \sum_{i=1}^n A_i e^{-t/\tau_i}$, where $I_{PL}(t)$ represents the PL spectra of τ_i is the decay time, and A_i is the amplitude.

3.3. Electron excitation analysis

The excited states of a HPW-based material are commonly supposed to be very important for involving the photocatalytic process, whereas the detailed electron excitation analysis of the materials have long been ignored. Given that it remains a challenge for instrumental analysis, collecting information of electron excitation was carried out using a computational approach based on TD-DFT, which is able to provide deep insight into electron transition problems [45]. The lowest excited singlet (S_1) state was selected as a representative and important excited state for photochemical properties to explore the distribution characteristics of photochemical and holes for Ch₃-HPW and HPW. The main parameters for the S_1 states analysis of the samples were listed in Table 1.

The calculated transition energies ($E_{S_0 \rightarrow S_1}$) from the ground state (S_0) to the S_1 state for Ch₃-HPW and HPW were 3.39 and 3.28 eV, respectively, which slightly larger than those of inferred from UV-vis. The integral of overlap of hole-electron distribution (I_o) is a measurement of spatial separation of hole and electron [46]. I_o values were 0.284 and 0.158 for Ch₃-HPW and HPW, respectively, suggesting that the spatial overlap between hole and electron of Ch₃-HPW is slightly larger than

that of HPW. The distance between centroid of hole and electron (D_c) is a measurement of charge-transfer length. The larger the value is, the longer length the charge transfers. D_c values were 0.07 and 0.428 Å for Ch₃-HPW and HPW, respectively, which imply that the charge transition distance in Ch₃-HPW is obviously shorter than that of HPW. In general, E_b value could be predicted by the product of the numbers of localized valence and conduction states near band edges in previous reports [21], which is a relatively time-consuming approach. Here, assuming that “electrons” of course carry negative charge and “holes” can be regarded as carrying positive charge, the E_c value can be easily estimated and the E_b value can be further calculated. The calculated E_b values were 26.0 and 18.9 meV for Ch₃-HPW and HPW, respectively, implying Ch₃-HPW has the slightly stronger excitonic effects than HPW. Hence, as a powerful complementary to the spectral observation, the calculated parameters of excited states further verify the existence of slightly enhanced electron-hole interaction in Ch₃-HPW relative to HPW.

Fig. 4a depicts electron and hole distributions in the S_1 states of Ch₃-HPW and HPW. The visualized isosurfaces clearly show that electron (green) and hole (purple) distributions are located in W_{5d} and O_{2p} orbitals, respectively. This also confirms that the charge transfer from O_{2p} to W_{5d} orbitals are speculated from UV-vis DRS. The transition density matrix (TDM) is a useful tool for providing a straightforward characteristic spatial map which indicates the distribution of the associated electron-hole pairs and allowing one to identify their delocalization and coherence lengths [47]. As shown in Fig. 4b, it was clearly that the $S_0 \rightarrow S_1$ transition only involves $O_{b/c}$ and W atoms for HPW and Ch₃-HPW, while O, N, and C atoms in Ch part almost didn't participated in. This indicates that the scope of the atoms involved in the $S_0 \rightarrow S_1$ transition between HPW and Ch₃-HPW are consistent. However, the degree of

Table 1

Selected parameters for electron excitation analysis of samples at B3LYP/lanl2dz for W atom and B3LYP/6-31 g (d, p) for P, C, N, O, and H atoms in vacuum.

	$E_{S_0 \rightarrow S_1}$ (eV)	I_o	D_c	E_c (eV)	E_b (meV)
HPW	3.28	0.158	0.428	-3.05	18.9
Ch ₃ -HPW	3.39	0.284	0.070	-3.49	26.0

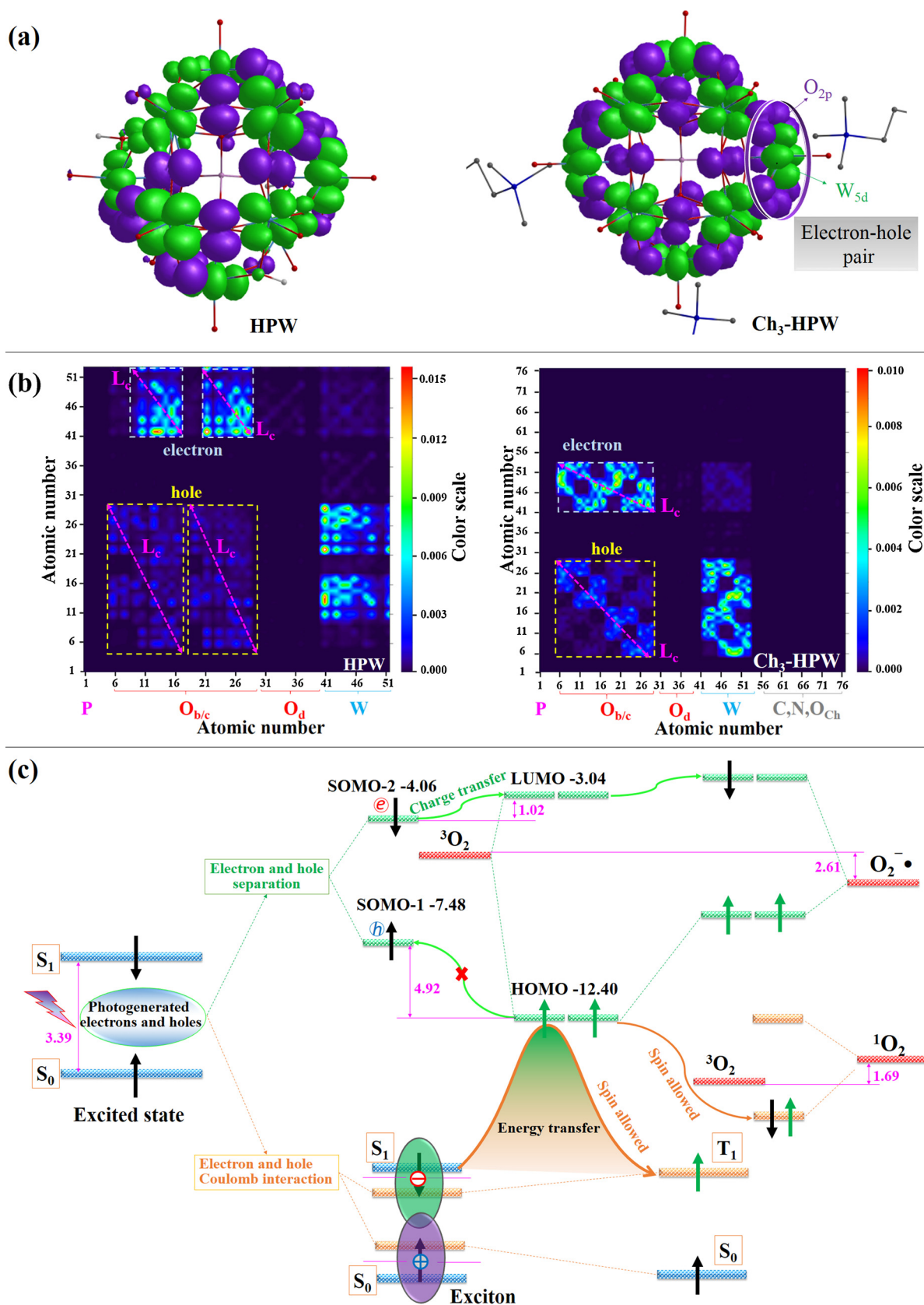


Fig. 4. (a) Hole and electron distributions and (b) TDMs for HPW and Ch₃-HPW at B3LYP/lanl2dz for W atom and B3LYP/6–31 g(d, p) for P, C, N, O, and H atoms in vacuum. (c) Channels for activation of molecular oxygen using Ch₃-HPW at B3LYP/lanl2dz for W atom and B3LYP/6–31 g(d, p) for P, C, N, O, and H atoms in MeCN (energy in eV).

delocalization of electrons and holes they formed is slightly different. This delocalization and interatomic correlation length can be described by the pink bidirectional arrows (L_c) in Fig. 4b. In the bare HPW, the distributions of electron or hole are more like two separate parts. In $\text{CH}_3\text{-HPW}$, the distribution of electron or hole can be regarded as a whole approximately, delocalized over the entire Keggin structure. This means that there may be a more pronounced Coulomb interaction between electron and hole.

To further clarify the role of excitons, the speculated route of $\text{CH}_3\text{-HPW}$ to activate the $^3\text{O}_2$ was depicted in Fig. 4c. The separation and Coulomb interactions between electrons and holes, which are two opposing channels, are considered together in the route. In the electron-hole separation channel, assuming that one spin electron is completely excited from the HOMO to the LUMO, the $\text{CH}_3\text{-HPW}$ forms two singly occupied molecular orbitals (SOMO) after obtaining an excitation energy of 3.39 eV. The energies of SOMO-1 and SOMO-2 were -7.48 and -4.06 eV, respectively. Obviously, the electron transfers from the HOMO of $^3\text{O}_2$ (-12.40 eV) to the SOMO-1 of $\text{CH}_3\text{-HPW}$ (-7.48 eV) is difficult to achieve because of a relative large energy difference (4.92 eV). Consequently, the charge transfer is more likely to occur between the SOMO-2 of $\text{CH}_3\text{-HPW}$ and the LUMO of $^3\text{O}_2$, thereby forming $\text{O}_2^{\cdot-}$, because electron only need to overcome the energy barrier of 1.02 eV in this process. In addition, when $^3\text{O}_2$ converts to $\text{O}_2^{\cdot-}$, it will release energy of 2.61 eV. So this is a thermodynamically permissible process. Therefore, the electron and hole separation channel has been received sufficient attention in most photocatalytic reactions [20,24].

Here, the electron-hole Coulomb interaction channel was additionally considered, because it played an important role. Tentatively assume that photons directly activate $^3\text{O}_2$ to form $^1\text{O}_2$, that is, $^3\text{O}_2(\uparrow\uparrow) \rightarrow ^1\text{O}_2(\uparrow\downarrow) - 1.69$ eV. This is an overcoming electron spin flipping process that requires an additional energy of 1.69 eV. According to the above experimental observation, the electrons and holes can form short-lived excitons with an E_b of 26 meV. Temporarily stable excitons will promote the following reaction via energy transfer: $\text{CH}_3\text{-HPW}(\text{S}_1) + ^3\text{O}_2 \rightarrow \text{CH}_3\text{-HPW}(\text{T}_1) + ^1\text{O}_2 - 1.16$ eV. This is a spin allowed process that only requires energy of 1.16 eV. Therefore, this process was an energetically favorable, instead of activating directly $^3\text{O}_2$ by photons. Further, we can tentatively speculate that $^1\text{O}_2$ will become a major ROS responsible for the following desulfurization reactions.

According to the above observations, we confirmed that there is a slightly enhanced excitonic effect in $\text{CH}_3\text{-HPW}$. In this case, in addition to the traditional view of a photogenerated charge carrier based on the band gap theory, the electron-hole interaction must also be considered because it can generate $^1\text{O}_2$ through energy transfer.

3.4. DBT removal in different reaction systems

By virtue of the intriguing electrons and holes interaction behavior, $\text{CH}_3\text{-HPW}$ is expected to exhibit excellent photocatalytic performance for the PDS reaction. Fig. 5a depicts the removal of DBT from model oil in different reaction systems. Sulfur removal with air as the oxidant was 10.5% and 25.6%, respectively, under the reaction condition of only UV radiation and of only MeCN extraction. The sulfur removal was still quite low of 29.8% in 3 h even with simultaneous UV radiation and MeCN extraction. With adding HPW to the model oil under UV radiation, sulfur removal reached 76.5% (S content > 100 ppm) in 3 h, but the approach still failed to reach deep desulfurization [48]. However, when $\text{CH}_3\text{-HPW}$ was added to the above system, sulfur removal increased significantly, reaching 99.6% (S content < 5 ppm) and achieving deep desulfurization. When MeCN was absent from the system, sulfur removal decreased sharply to 10.9%. This was reasonable because it is difficult to form ROS in the oil phase with a small amount of oxygen compared to that in MeCN, which inhibited the catalytic activity of $\text{CH}_3\text{-HPW}$. When air-bubbling was replaced by N_2 -bubbling in the EPODS system, sulfur removal dramatically decreased to 33.4%.

Overall, these results indicate that the formation of a photocatalytic system by $\text{CH}_3\text{-HPW}$ is more favorable than that of pure HPW in promoting the removal of DBT from model oil under UV radiation. Additionally, both MeCN as the extractant and O_2 as the oxidant play important roles in the desulfurization reaction process.

Fig. 5a also presents that $\text{CH}_3\text{-HPW}$ has better desulfurization activity than HPW. The introduction of Ch would caused the increase in hydrophobicity of HPW due to the presence of short carbon chains. The static water contact angle (WCA) was 87.5° for $\text{CH}_3\text{-HPW}$ (Fig. 5b), further confirming that its surface has more hydrophobic character. Noticeable, some obvious emulsion droplets were formed in the $\text{CH}_3\text{-HPW}$ system (Fig. 5c) during reaction, while they were hardly observed in the HPW system. Typically, the emulsion droplets consist of MeCN, model oil, and catalyst $\text{CH}_3\text{-HPW}$ [49], which provides a reaction microenvironment, enhancing the encounter chances between the catalyst and DBT in the oil. Thus, compared with pristine HPW, $\text{CH}_3\text{-HPW}$ enhanced the lipophilicity performance, which provides a higher degree of exposure of the catalytic sites to the model oil [50].

3.5. Effects of reaction conditions on sulfur removal

Fig. 6a shows the effect of the amount of $\text{CH}_3\text{-HPW}$ on the removal of DBT. Sulfur removal gradually increased with an increasing amount of $\text{CH}_3\text{-HPW}$ from 6 to 12 mg and reached a maximum of 99.6% in 3 h when the $\text{CH}_3\text{-HPW}$ dosage was 12 mg. When the amount of $\text{CH}_3\text{-HPW}$ was further increased to 15 mg, sulfur removal decreased. This phenomenon that the amount of catalyst presents an upper limit value has long been observed in previous photocatalytic reactions [51,52]. This is reasonable because the excessive introduction of $\text{CH}_3\text{-HPW}$ can lead to a significant increase in the opacity of the MeCN phase, which reduces the light absorption by the reaction system. Therefore, 12 mg $\text{CH}_3\text{-HPW}$ was chosen as the most suitable amount in the following investigation, and this was a relatively low catalyst dosage (0.8 g/L) compared with other metal-containing photocatalysts [14,18].

Fig. 6b shows the effect of volume ratio of MeCN to model oil (M/O) on the removal of DBT. It is clear that the amount of MeCN had a significant influence on the removal of DBT. When M/O was increased from 1:6 to 1:2, a gradual increase in the removal of DBT was observed. Only 89.8% of the DBT was removed from the model oil at $M/O = 1:6$, while almost all of the DBT was removed within 3 h at $M/O = 1:2$. This implied that the increase in the amount of MeCN improved the mass transfer effects between the oil and the extraction phases. The optimum sulfur removal can be obtained under the conditions of M/O of 1:2. Continuing to increase M/O to 1:1.5, however, resulted in a slight decrease in the removal of DBT. This suggested that the final sulfur removal depended not only on the mass transfer rate between the oil and the MeCN phases, but also on the other factors affecting the reaction rate in MeCN phase, such as the dissolved O_2 diffusion rate and the free radicals concentration.

Fig. 6c shows the effect of air/ N_2 bubbling flow rate on the removal of DBT. Sulfur removal was dramatically facilitated by the air bubbling but was suppressed by N_2 bubbling. At a N_2 flow rate of 20 mL min^{-1} , the sulfur removal of DBT sharply decreased to 33.4%, indicating that DBT could not be oxidized and was only extracted by MeCN. In the case of no air bubbling, the sulfur removal was still as high as 96.5%, and this was mainly attributed to the enough dissolved O_2 in MeCN. An increase in the air flow rate from 20 to 40 mL min^{-1} caused almost no increase in the sulfur removal because of the introduction of sufficient O_2 into the reaction system at a lower air inflow rate. These observations demonstrated that O_2 plays a vital role in the formation of ROS to further oxidize sulfur compounds, and this is consistent with the observed results reported in other aerobic ODS systems [53–55].

The initial concentration of sulfur compounds cannot be neglected in considering the deep desulfurization of various fuel oils in practical processes. Fig. 6d shows the effect of the initial DBT concentration on sulfur removal. The sulfur removal slightly decreased when the initial

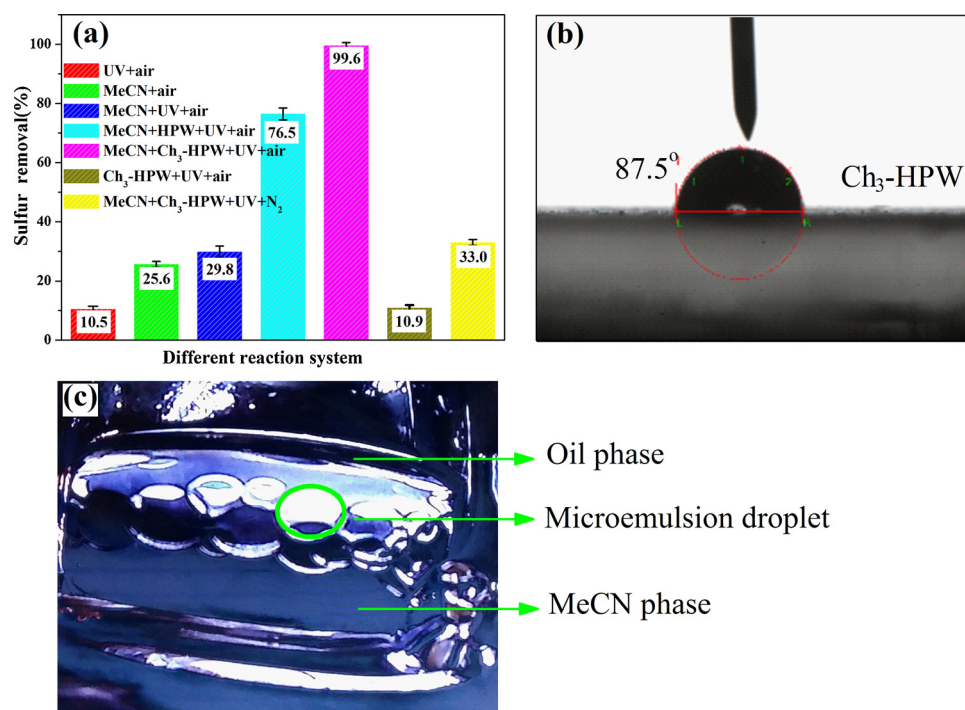


Fig. 5. (a) Sulfur removal Desulfurization rate from model oil using different photocatalytic desulfurization systems. Experimental conditions: m (cat.) = 12 mg, T = 30 °C, V (model oil) = 15 mL, volume ratio of MeCN to model oil (M/O) = 1:2 or none, C_0 (DBT) = 500 ppm, t = 3 h, and v (air or N₂) = 20 mL min⁻¹. (b) WCA for Ch₃-HPW. (c) Optical image of Ch₃-HPW reaction system within 30 s after stopping the stirring.

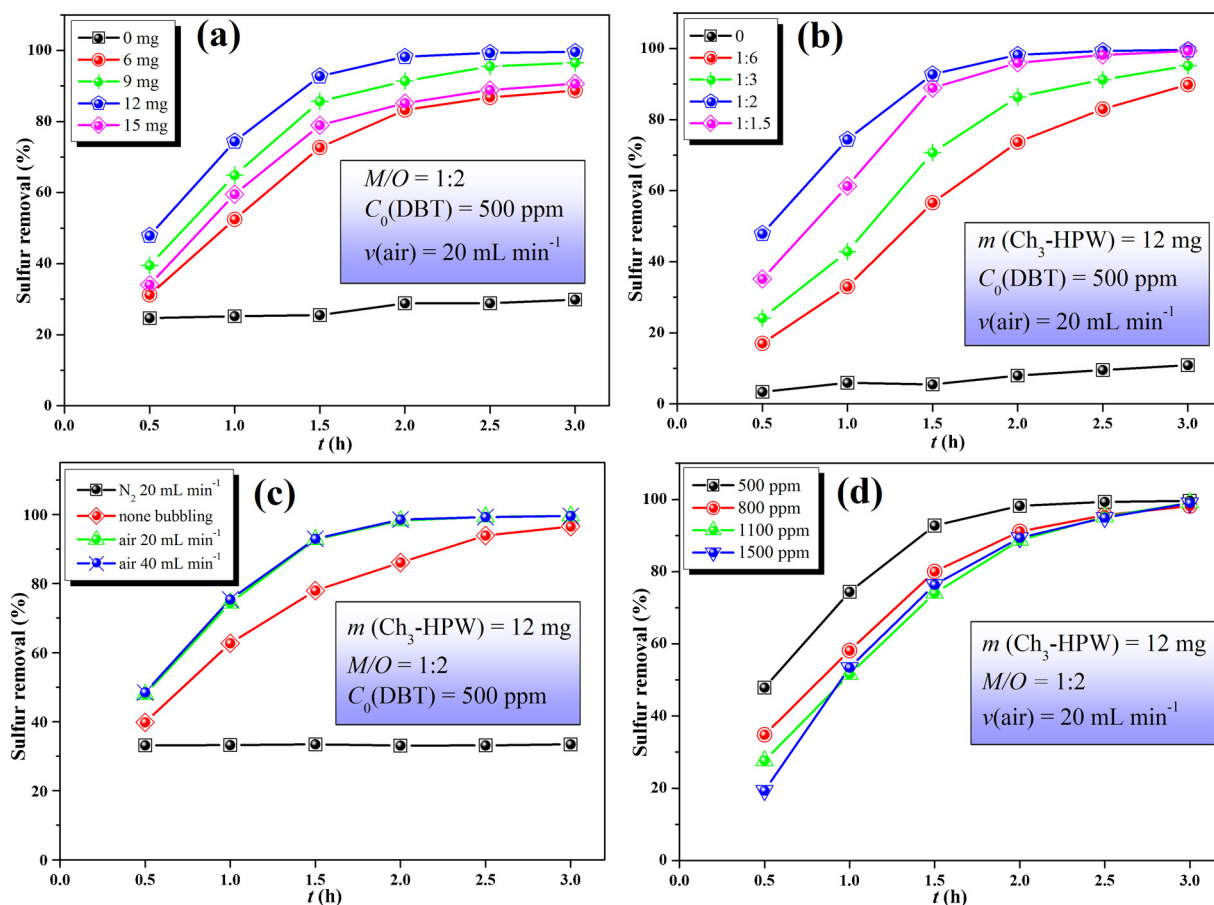


Fig. 6. Effects on the removal of DBT by (a) the amount of Ch₃-HPW, (b) the M/O , (c) the air/N₂ bubbling, and (d) the initial S-concentration. Other identical experimental conditions: T = 30 °C and V (model oil) = 15 mL.

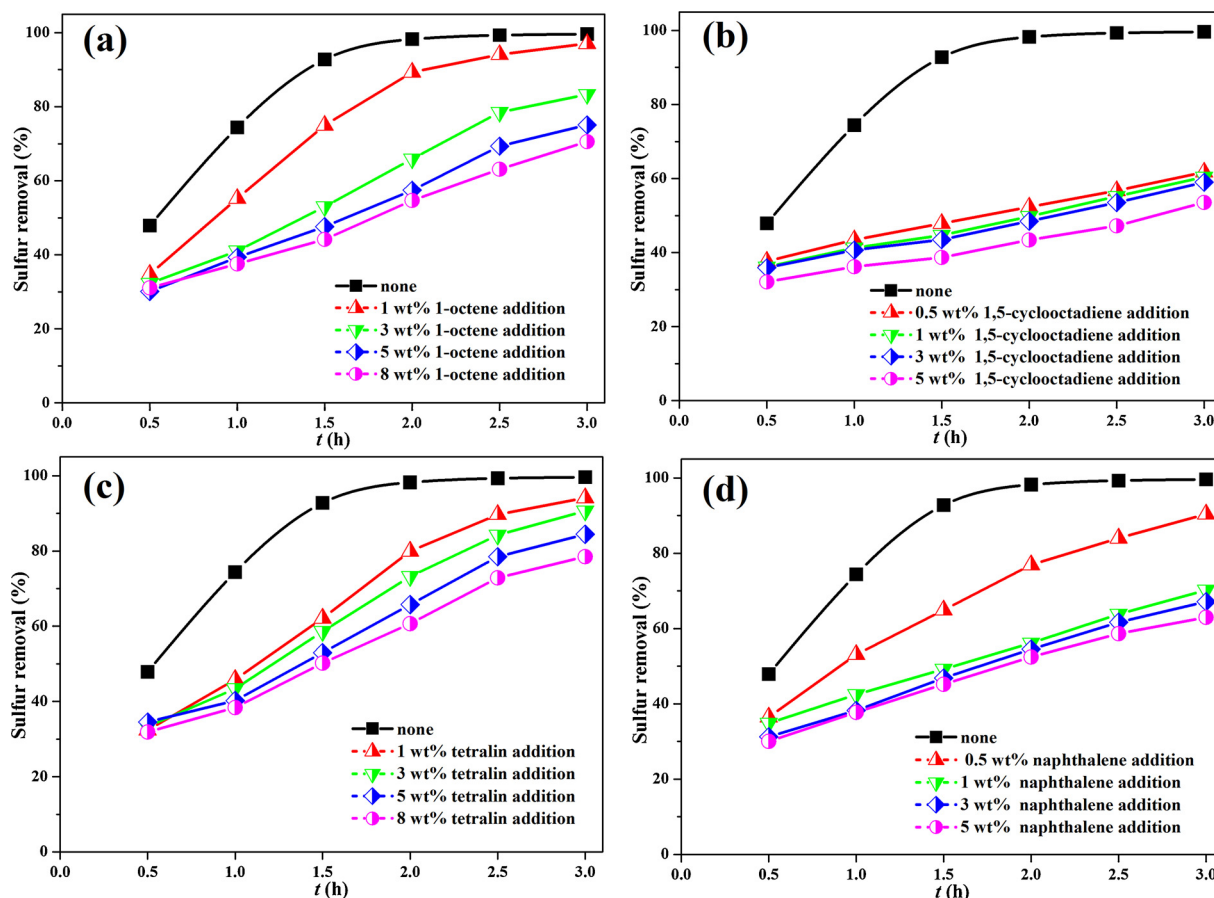


Fig. 7. Effects of the amount of (a) 1-octene, (b) 1,5-cyclooctadiene, (c) tetralin, and (d) naphthalene on sulfur removal from model oil. Experimental conditions: $T = 30^\circ\text{C}$, $V(\text{model oil}) = 15\text{ mL}$, $C_0(\text{DBT}) = 500\text{ ppm}$, $m(\text{CH}_3\text{-HPW}) = 12\text{ mg}$, $M/O = 1:2$, and $v(\text{air}) = 20\text{ mL min}^{-1}$.

concentration of DBT was increased from 500 ppm to 1100 ppm. In particular, the sulfur removal still reached 98.9% in 3 h with a high initial S-concentration of 1500 ppm, which was difficult to achieve in the TiO_2 photocatalytic desulfurization system [56]. In addition, the sulfur removal in the current reaction system at the higher initial DBT concentration was also slightly better than that of in the photochemical ODS system of isobutyraldehyde [55]. Thus, this may provide a potential technology for the deep desulfurization for high S-content oils.

3.6. Effects of fuel composition on sulfur removal

Real oil contains a certain amount of olefins and aromatic hydrocarbons, consisting of mono-, di-, and polycyclic olefins and aromatics that depress the photocatalytic reaction of HASCs [57,58]. Consequently, 1-octene, 1,5-cyclooctadiene, tetralin, and naphthalene were chosen as representative mono-olefin, dicyclic-olefin, mono-aromatic, and dicyclic-aromatic, respectively, to investigate their effects on the removal of DBT. Polycyclic aromatics were not considered herein, because their content in fuels is strictly limited according to China V fuel quality standards. As shown in Fig. 7a, the sulfur removal after 3 h of reaction was 97.1%, 83.3%, 75.1%, and 70.6% with the addition of 1 wt%, 3 wt%, 5 wt%, and 8 wt% 1-octene, respectively. Sulfur removal decreased slightly with an increasing concentration of 1-octene. As shown in Fig. 7b, the sulfur removal after 3 h of reaction was 61.7%, 60.4%, 58.9%, and 53.5% with the addition of 0.5 wt%, 1 wt%, 3 wt%, and 5 wt% 1,5-cyclooctadiene, respectively. These observations indicate that dicyclic-olefins inhibit the sulfur removal more strongly than mono-olefins.

As shown in Fig. 7c, the sulfur removal after 3 h of reaction was 94.1%, 90.6%, 84.4%, and 78.5% with the addition of 1 wt%, 3 wt%,

5 wt%, and 8 wt% tetralin, respectively. Sulfur removal decreased slightly with an increasing concentration of tetralin. As shown in Fig. 7d, the sulfur removal after 3 h of reaction was 90.4%, 70.2%, 67.1%, and 62.9% with the addition of 0.5 wt%, 1 wt%, 3 wt%, and 5 wt% naphthalene, respectively. Compared to the tetralin addition, sulfur removal decreased remarkably with an increasing concentration of naphthalene. This is because a triplet-energy transfer from the photoexcited DBT to the ground-state naphthalene occurred [58]. Consequently, the photooxidation of DBT was suppressed more strongly by naphthalene. Although prolonging the reaction time further, the final sulfur removal slowly increase with the successive photodecomposition of naphthalene, it was a time-consuming and energy-consuming measure. Therefore, dicyclic-olefin and dicyclic aromatics should be separated prior to UV irradiation based on the current method to achieve efficient deep desulfurization. Or, this method is more suitable for oils with low content of olefins and aromatics, such as SRG.

3.7. Oxidation reactivities of different sulfur compounds

It is well known that BT and DBT account for more than 50% of the total sulfur in diesel fuel, whereas the largest fraction of HASCs present in low-sulfur diesel fuels are C2-DBTs such as 4,6-DMDBT [59]. Consequently, investigating the oxidation reactivities of HASCs is important for designing the reaction process in industrial applications. In the previous thermal and photocatalytic systems, because of the electronic structure and steric hindrance effects of sulfur compounds, the desulfurization rates of different sulfur compounds are significantly different. In particular, 4,6-DMDBT, which has a significant steric hindrance effect, is generally not well removed. As shown in Fig. 8a, the sulfur removal of BT, DBT, 4-MDBT, and 4,6-DMDBT reached 100%,

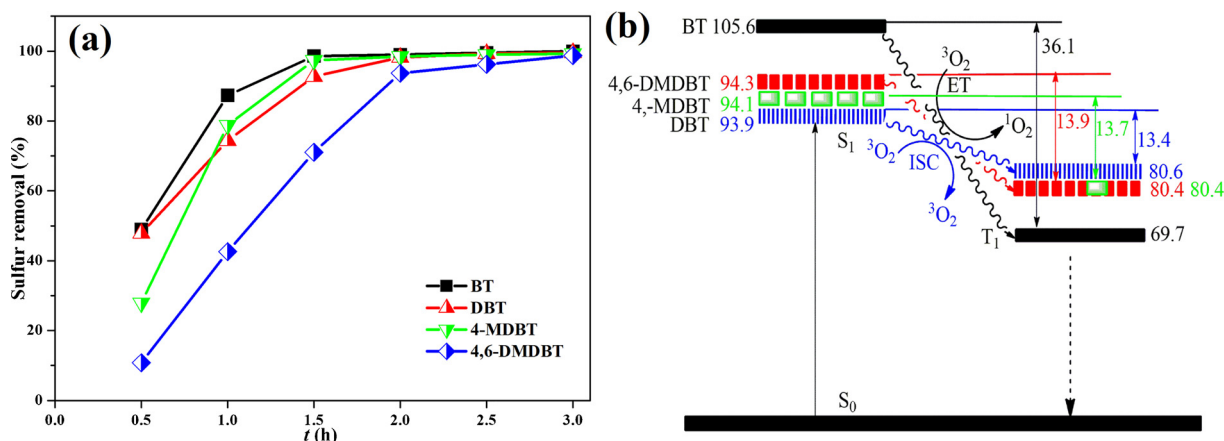


Fig. 8. (a) Effects of different substrates on sulfur removal. Experimental conditions: $T = 30\text{ }^{\circ}\text{C}$, $V(\text{model oil}) = 15\text{ mL}$, $C_0(\text{S}) = 500\text{ ppm}$, $m(\text{Ch}_3\text{-HPW}) = 12\text{ mg}$, $M/O = 1:2$, and $v(\text{air}) = 20\text{ mL min}^{-1}$. (b) Relative energies (in kcal mol^{-1}) of excited states using B3LYP/6-311 + G(d, p) in MeCN. ET: Energy transfer and ISC: Intersystem crossing.

99.6%, 99.3%, and 98.7% in 3 h, respectively, indicating the current system has excellent removal efficiency for these refractory sulfur compounds. Meanwhile the reactivities of BT, DBT, 4-MDBT, and 4,6-DMDBT are close, which is favorable for industrial production.

To further understand the nature of the reactivities of these sulfur compounds, the energies of the frontier molecular orbital (FMO) and transition energies of each compound were analyzed by the DFT method, as shown in Table S2 in SI. The energies of HOMOs of BT, DBT, 4-MDBT, and 4,6-DMDBT were -6.28 , -6.22 , -6.17 , and -6.13 eV , respectively, suggesting that their abilities to provide electrons increase in that sequence. Based on this result, it is speculated that the reactivity should follow the order: $\text{BT} < \text{DBT} < 4\text{-MDBT} < 4,6\text{-DMDBT}$, which is contrary to the experimental observations in the current system. According to our previous report [52], $^3\text{O}_2$ may also be activated to $^1\text{O}_2$ through the energy transfer of sulfur compound, but this requires the energy difference (ΔE_{ST}) between $\text{HASC}(\text{S}_1)$ and $\text{HASC}(\text{T}_1)$ was more than $22.4\text{ kcal mol}^{-1}$. As shown in Fig. 8b, ΔE_{ST} for BT, DBT, 4-MDBT, and 4,6-DMDBT are 36.1, 13.4, 13.7, and 13.9 kcal mol^{-1} , respectively, indicating that only BT(S_1) can interact with $^3\text{O}_2$ through energy transfer to yield $^1\text{O}_2$. Although BT has the weakest abilities to provide electrons, BT may obtain more $^1\text{O}_2$ through energy transfer, which is consistent with its observed highest reactivity. In addition, although 4,6-DMDBT has the strongest ability to provide electrons, it has the greatest steric hindrance. Therefore it shows the lowest reactivity in oxidation.

3.8. Proposed mechanism for the DBT photocatalytic oxidation process

According to the foregoing description, charge transfer and energy transfer channels may exist simultaneously in the photocatalytic activation of $^3\text{O}_2$ using $\text{Ch}_3\text{-HPW}$. The generation of $\text{O}_2^{\cdot-}$ and h^+ is considered to be related to the charge transfer channel, while the generation of $^1\text{O}_2$ is attributed to the energy transfer process [21]. Further, $\text{O}_2^{\cdot-}$ and h^+ react with unavoidable water in the air to produce hydroxyl radicals (HO^{\cdot}) and hydrogen peroxide (H_2O_2). Hence, it is possible that various potential ROS will participate in the desulfurization reaction.

To identify the involved ROS during the photocatalytic process of $\text{Ch}_3\text{-HPW}$, TBA, BQ, catalase, EDTA-2Na, and carotene were further selected, which are scavengers for HO^{\cdot} , $\text{O}_2^{\cdot-}$, H_2O_2 , h^+ , and $^1\text{O}_2$, respectively [23]. As shown in Fig. 9a, the sulfur removal of DBT was dramatically reduced to 49.2%, 44.4%, and 31.7% by adding catalase (10 mg mL^{-1}), EDTA-2Na (20 mM), and carotene (20 mM), respectively, suggesting that $^1\text{O}_2$, h^+ , and H_2O_2 are the chief active species in the oxidation of DBT. This differs from previous observations in the

degradation of dye Acid Orange 7 where $^1\text{O}_2$ only played a minor role [60]. Furthermore, the addition of TBA (20 mM) and BQ (20 mM) had relatively weak effects on desulfurization rate, which caused the sulfur removal of DBT to reduce to 95.9% and 91.7% respectively, implying that $\text{O}_2^{\cdot-}$ and HO^{\cdot} played a secondary role in this process.

ESR measurements were carried out to gain more direct proofs for the photogenerated ROS. 2,2,6,6-tetramethylpiperidine (TEMP) is employed as the trapping agents for $^1\text{O}_2$. As illustrated in Fig. 9b, no signal could be observed in the dark, which indicated that there was no chemisorption of O_2 on $\text{Ch}_3\text{-HPW}$ surfaces. After UV irradiation for 5 min, a 1:1:1 triplet signal with g -value of 2.00142 and $a^N = 1.72\text{ mT}$ arises in the presence of $\text{Ch}_3\text{-HPW}$, which can be indexed to the generation of 2,2,6,6-tetramethylpiperidine- N -oxyl (TEMPO) [21,61]. Clearly, triplet ESR signal becomes very strong after UV irradiation for 10 min, which shows that the $^1\text{O}_2$ presents a relatively high concentration in reaction system. In the previous aqueous solution, only a relatively low yield of $^1\text{O}_2$ was observed even on the surface modification of TiO_2 [62]. Furthermore, the ESR spectra with 5,5-dimethyl-1-pyrroline- N -oxide (DMPO) (Fig. 9c) exhibit typical signals with characteristic intensity of 1:2:2:1 ($a^N = 1.5\text{ mT}$, $a^{\beta\text{-H}} = 1.48\text{ mT}$), is assigned to the HO^{\cdot} adduct of DMPO [63]. No obvious ESR signals of h^+ and H_2O_2 were observed, which does not contradict with the radicals scavenger experiments. h^+ mainly generate HO^{\cdot} by oxidation of water, and H_2O_2 involved eventually in the desulfurization reaction was further obtained by HO^{\cdot} dimerization [64,65].

To accurately describe the differences in reactivity between ROS and DBT, the energies of the FMOs of ROS and DBT were computed and are shown in Fig. 9d. According to FMO theory, it is known that the reactivity between two molecules is inversely proportional to the energy difference ($\Delta E_{\text{L-H}}$) between the LUMO of one molecule and the HOMO of the other. The smaller the value of $\Delta E_{\text{L-H}}$ is, the more reactive the chemical reaction is. Clearly, $\Delta E_{\text{L-H}}$ subtracted the HOMO energy of DBT from the LUMO energies of $^1\text{O}_2$, H_2O_2 , HO^{\cdot} , and $\text{O}_2^{\cdot-}$, were 0.95, 5.80, 7.28, and 8.09 eV, respectively. The reaction trend still shows that the reactivity of $^1\text{O}_2$, H_2O_2 , HO^{\cdot} , and $\text{O}_2^{\cdot-}$ with DBT decreases sequentially in these active radicals. $^1\text{O}_2$ has the greatest reactivity. According to the principle of energy closeness, if two molecules are to form chemical bonds, $\Delta E_{\text{L-H}}$ cannot exceed 6 eV in general. Therefore, it is further suggested that HO^{\cdot} and $\text{O}_2^{\cdot-}$ are difficult to react with DBT directly because of their large energy barriers. However, notably, $\Delta E_{\text{L-H}}$ subtracted the HOMO energy of $\text{O}_2^{\cdot-}$ from the LUMO energy of DBT was 2.86 eV, which imply that $\text{O}_2^{\cdot-}$ is more likely to provide electrons to the DBT in the current reaction than to accept electrons. However, the LUMO of DBT and the HOMO of $\text{O}_2^{\cdot-}$ are both the π antibonding orbitals (π^*), and this electron transfer is usually

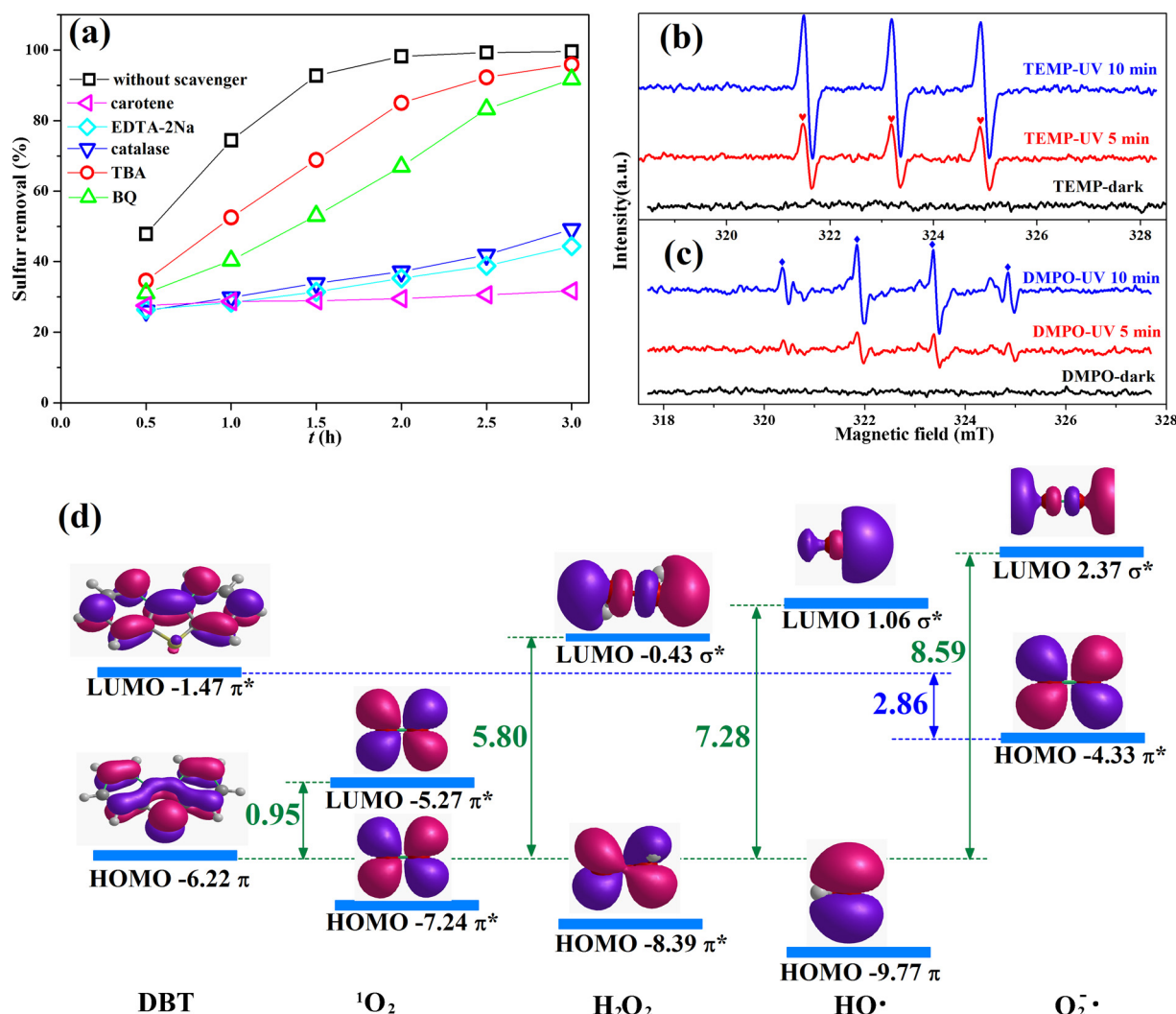


Fig. 9. (a) Effects of scavengers on the removal of DBT. Experimental conditions: $T = 30^\circ\text{C}$, $V(\text{model oil}) = 15\text{ mL}$, $C_0(\text{S}) = 500\text{ ppm}$, $m(\text{Ch}_3\text{-HPW}) = 12\text{ mg}$, $M/O = 1:2$, $v(\text{air}) = 20\text{ mL min}^{-1}$, and $c(\text{carotene}) = 20\text{ mM}$ or, $c(\text{catalase}, \geq 200,000\text{ unit g}^{-1}) = 10\text{ mg mL}^{-1}$ or, $c(\text{EDTA-2Na}) = 20\text{ mM}$ or, $c(\text{TBA}) = 20\text{ mM}$ or, $c(\text{BQ}) = 20\text{ mM}$ or without scavenger. ESR spectra with (b) TEMP and (c) DMPO for the reaction system under UV radiation. (d) Energies (in eV) and isosurfaces of the HOMOs and the LUMOs of ROS and DBT at theoretical level of B3LYP/6-311 + g(d, p) in MeCN. Only the alpha molecular orbital was adopted for $\text{HO}\cdot$ and $\text{O}_2^{\cdot-}$.

difficult to occur. Therefore, $\text{O}_2^{\cdot-}$ may be inclined to follow the classic conversion path, such as further generating H_2O_2 with trace amounts of water in the air instead of directly reacting with DBT.

The DFT calculation results further confirmed that $^1\text{O}_2$ and H_2O_2 acted as the main active species in the oxidation of DBT, which is in good agreement with the aforementioned scavenger experiments and the observed ESR signal.

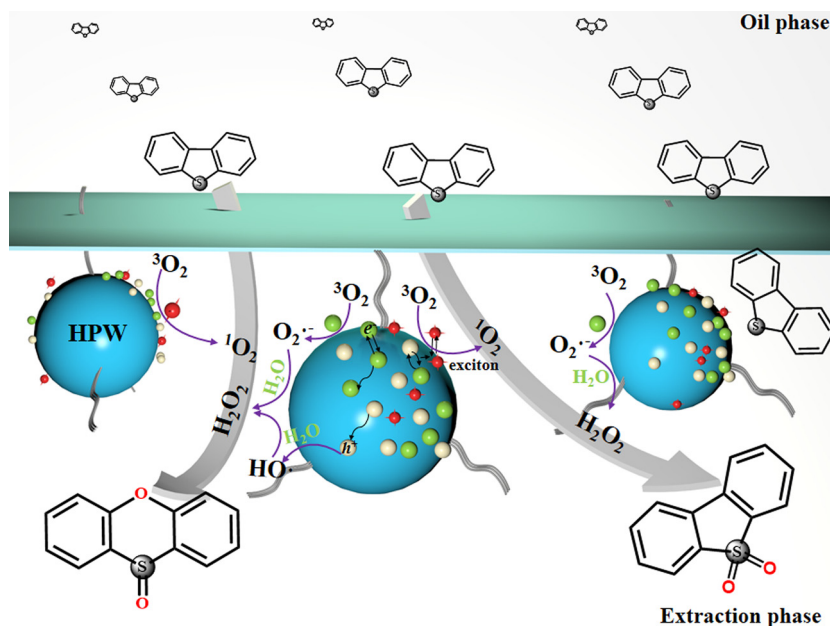
After reaction, the MeCN phase was separated and diluted 10 times with methanol to study the photocatalytic oxidizing products using GC-MS. As shown in Fig. S6 in SI, there are several peaks in the total ion chromatogram, indicating that complicated products were obtained by the oxidation of DBT. According to the mass spectra, the molecular ion peaks of the two main compounds at 10.69 min and 11.23 min were attributed to phenoxathiine 10-oxide (DBTO₂-1) and dibenzo[b,d] thiophene 5,5-dioxide (DBTO₂-2), respectively, although other peaks could not be clearly identified. DBTO₂-2 is commonly referred to as dibenzothiophene sulfone, which has been a frequently observed product in previous thermos-catalytic or photocatalytic ODS studies [53,55,66].

Based on the above-mentioned results of ESR, DFT, and GC-MS analyses, a proposed mechanism is depicted in Scheme 1. The model oil, $\text{Ch}_3\text{-HPW}$, and MeCN formed a lipophilic catalytic system. At the

beginning of reaction, DBT was initially extracted into the MeCN phase and then oxidized by $^1\text{O}_2$ and H_2O_2 . The stepwise oxidation mechanism for the reactions process has been widely accepted by previous studies [55,67]. DBT is first oxidized to the corresponding sulfoxide (DBTO) by $^1\text{O}_2$, H_2O_2 , and $h\nu$, and then to DBTO₂-1 and DBTO₂-2, which remain in the MeCN phase because of their high polarity. Ultra-low sulfur model oil was obtained when DBT was transferred from the oil phase to the MeCN phase and continuously oxidized to DBTO₂.

3.9. Desulfurization of real oil

According to the aforementioned results, the desulfurization effect of the present method is limited by the contents of the olefins and aromatics. Consequently, it is not suitable for high olefins and aromatics oil fractions, such as fluidized catalytically cracked gasoline with an olefin content of more than 30 wt%. Therefore, SRG with high paraffin content and low olefin content was chosen as a representative of real oils [68]. SRG is an important feedstock of ethylene cracking and blending gasoline, and its sulfur content is also severely limited. However, the sulfur content (100–700 ppm) of SRG is not a stable value, which depends strongly on the quality of the crude oil. For comparison with the model oil, an appreciate amounts of thiophene and



Scheme 1. Schematic depiction of the desulfurization process using $\text{Ch}_3\text{-HPW}$ in the presence of O_2 under UV radiation.

Table 2
Contents of key components in the SRG during desulfurization.^a

	Before desulfurization	After desulfurization
Sulfur (ppm)	432	42
Paraffin (wt%)	65.4	65.1
Naphthenic (wt%)	24.7	26.1
Aromatic (wt%)	9.8	8.9
Olefin (wt%)	/	/

^a Experimental conditions: $T = 30^\circ\text{C}$, $V(\text{SRG}) = 15\text{ mL}$, $m(\text{Ch}_3\text{-HPW}) = 12\text{ mg}$, $M/O = 1:2$, and $v(\text{air}) = 20\text{ mL min}^{-1}$.

benzothiophene were added to the SRG obtained from the refinery to adjust its initial sulfur content to 432 ppm. Then, the extraction and photocatalytic desulfurization of SRG was carried out. Under the optimal reaction conditions, the sulfur content of SRG was reduced to 42 ppm (Table 2) after 3 h of irradiation. The sulfur removal was only 89.9%, which suggested that the desulfurization were significantly reduced in the SRG. Therefore, it is necessary to understand the hydrocarbon composition data in SRG, which is an important technical indicator affecting its performances and applications.

To understand the effect of this photocatalytic reaction on oil composition, PONA contents in SRG were further determined, the summarized data given in Table 2 and the contents of detailed hydrocarbons given in Tables S3–S5 in SI. These results showed that paraffins were hardly involved in the desulfurization reaction because of their relatively high C–C bond dissociation energy (about 80 kcal mol^{-1}) and $\sigma \rightarrow \sigma^*$ orbital gap energy (more than 143 kcal mol^{-1}). The slight decrease in paraffins could be attributed to MeCN extraction and volatilization losses during the reaction. Meanwhile, the contents of naphthenes in SRG increased significantly from 24.7% to 26.1% while the contents of aromatics slightly decreased from 9.8% to 8.9% after the photocatalytic desulfurization. This result was also consistent with the observations that bicyclic aromatic hydrocarbon content decreased by 0.3% in kerosene photooxidation desulfurization reported by Tao et al. [69]. This is mainly due to the favorable $\pi \rightarrow \pi^*$ transition of polycyclic aromatics and the formation of a more active excited state under UV irradiation. On the one hand, the delocalization of the π^* orbitals leads to the α or β cleavage of alkylaromatics and the production of light olefins [70]. The generated olefins further form naphthenes by a photocyclization reaction with aromatics. On the other hand, the photo-

isomerization of the low-carbon aromatics generates olefins and further forms naphthenes. For instance, the excited benzene can form its valence tautomers such as benzvalene and fulvene, which can be further generated oxygenated cycloalkanes by additional reaction with ROS. However, the oxygenated cycloalkanes have not been completely identified because a limited hydrocarbon database was used in the current work.

On the whole, some unexpected side reactions may occur due to the complexity of the real oil composition. In particular, the competitive reaction of aromatics in SRG not only inhibited the sulfur removal, but also affected the hydrocarbon composition of the oil. Although Xie et al. [21] proposed that photogenerated $^1\text{O}_2$ can selectively oxidize sulfides in fuels, the photo activation of aromatics under irradiation was also an important reason for the decrease of selectivity. Therefore, controlling the generation of specific free radicals or using a constant wavelength light source might provide a solution to the problem of selectivity in photocatalytic desulfurization system.

4. Conclusions

In summary, $\text{Ch}_3\text{-HPW}$ had slightly enhanced electron-hole interactions compared to bare HPW, and the induced excitonic effect played a key role in photocatalytic molecular oxygen activation. Activation of $^3\text{O}_2$ in electron and hole interaction channel leads to the formation of $^1\text{O}_2$, while H_2O_2 and h^+ originated from electron and hole separation channel. Then, an efficient extraction and photocatalytic oxidation desulfurization (EPODS) system for fuel oil was successfully developed, on the basis of $\text{Ch}_3\text{-HPW}$, air, and MeCN. The main reaction conditions were assessed, including the amount of $\text{Ch}_3\text{-HPW}$, the volume ratio of MeCN to model oil, the initial S-concentration, air/ N_2 bubbling, different sulfur compounds, and fuel composition. The results demonstrated that the EPODS had an optimal photocatalytic performance with a $\text{Ch}_3\text{-HPW}$ dosage of 12 mg, M/O of 1:2, and air at a rate of 20 mL min^{-1} . Sulfur removal of BT, DBT, 4-MDBT, and 4,6-DMDBT were 100%, 99.6%, 99.3%, and 98.7%, respectively, in 3 h. The corresponding reactivity differences were attributed to the influences of both excitation energies and steric hindrance. $^1\text{O}_2$, H_2O_2 , and h^+ were responsible for the oxidation of sulfur containing compounds. The sulfur removal of SRG was reduced to 89.9%, mainly because the complexity of real oil caused some unexpected side effects. The work not only enables us to gain more comprehensive understandings on the exciton-

involved photocatalytic processes of HPA-based photocatalysts, but also opens up a new way for the desulfurization of liquid fuels using green and inexpensive O₂.

Acknowledgements

The work reported here was supported by the National Natural Science Foundation of China (Grant No. 21376099, 21403038, 21546002, 21878115), the Natural Science Foundation of Guangdong Province (Grant No. 2015A030313892), the Training Program for Outstanding Young Teachers in Colleges and Universities in Guangdong Province (Grant No. YQ2015116), and Petrochemical Industry Transformation and Upgrading Technology Innovation Public Service Platform in Maoming City (2016B020211002).

Appendix A. Supplementary data

Supplementary material related to this article can be found, in the online version, at doi: <https://doi.org/10.1016/j.apcatb.2018.09.038>.

References

- [1] J. Xiao, S. Sitamraju, Y. Chen, S. Watanabe, M. Fujii, M. Janik, C. Song, *AIChE J.* 61 (2015) 631–639.
- [2] Z. Vit, D. Gulkova, L. Kaluza, J. Kupcik, *Appl. Catal. B Environ.* 179 (2015) 44–53.
- [3] A.A. Toutov, M. Salata, A. Fedorov, Y.F. Yang, Y. Liang, R. Cariou, K.N. Betz, E.P.A. Couzijn, J.W. Shabaker, K.N. Houk, R.H. Grubbs, *Nat. Energy* 2 (2017) 17008.
- [4] Y.S. Al-Degs, A.H. El-Sheikh, R.Z. Al Bakain, A.P. Newman, M.A. Al-Ghouti, *Energy Technol.* 4 (2016) 679–699.
- [5] X. Meng, L. Li, K. Li, P. Zhou, H. Zhang, J. Jia, T. Sun, *J. Clean. Prod.* 176 (2018) 391–398.
- [6] Z. Li, D. Liu, Z. Men, L. Song, Y. Lv, P. Wu, B. Lou, Y. Zhang, N. Shi, Q. Chen, *Green Chem.* 20 (2018) 3112–3120.
- [7] N.A. Khan, B.N. Bhadra, S.H. Jung, *Chem. Eng. J.* 334 (2018) 2215–2221.
- [8] C. Yang, H. Ji, C. Chen, W. Ma, J. Zhao, *Appl. Catal. B: Environ.* 235 (2018) 207–213.
- [9] X. Li, F. Li, X. Lu, S. Zuo, C. Yao, C. Ni, *J. Alloy. Compd.* 709 (2017) 285–292.
- [10] D. Julião, A.C. Gomes, M. Pillinger, R. Valença, J.C. Ribeiro, I.S. Gonçalves, S.S. Balula, *Appl. Catal. B: Environ.* 230 (2018) 177–183.
- [11] A. Samokhvalov, *ChemPhysChem* 12 (2011) 2870–2885.
- [12] X. Wang, F. Li, J. Liu, C. Kou, Y. Zhao, Y. Hao, D. Zhao, *Energy Fuel* 26 (2012) 6777–6782.
- [13] X. Li, Y. Xu, C. Zhang, H. Wang, Y. Song, W. Zhang, C. Li, *Fuel* 226 (2018) 527–535.
- [14] H.F. Mohd Zaid, F.K. Chong, M.I. Abdul Mutalib, *Fuel* 156 (2015) 54–62.
- [15] X. Lu, X. Li, J. Qian, N. Miao, C. Yao, Z. Chen, *J. Alloy. Compd.* 661 (2016) 363–371.
- [16] X. Li, W. Zhu, X. Lu, S. Zuo, C. Yao, C. Ni, *Chem. Eng. J.* 326 (2017) 87–98.
- [17] F. Lin, Y. Zhang, L. Wang, Y. Zhang, D. Wang, M. Yang, J. Yang, B. Zhang, Z. Jiang, C. Li, *Appl. Catal. B: Environ.* 127 (2012) 363–370.
- [18] F. Lin, D. Wang, Z. Jiang, Y. Ma, J. Li, R. Li, C. Li, *Energy Environ. Sci.* 5 (2012) 6400–6406.
- [19] F. Lin, Z. Jiang, N. Tang, C. Zhang, Z. Chen, T. Liu, B. Dong, *Appl. Catal. B: Environ.* 188 (2016) 253–258.
- [20] S.S. Wang, G.Y. Yang, *Chem. Rev.* 115 (2015) 4893–4962.
- [21] H. Wang, S. Chen, D. Yong, X. Zhang, S. Li, W. Shao, X. Sun, B. Pan, Y. Xie, *J. Am. Chem. Soc.* 139 (2017) 4737–4742.
- [22] H. Wang, X. Sun, D. Li, X. Zhang, S. Chen, W. Shao, Y. Tian, Y. Xie, *J. Am. Chem. Soc.* 139 (2017) 2468–2473.
- [23] H. Wang, D. Yong, S. Chen, S. Jiang, X. Zhang, W. Shao, Q. Zhang, W. Yan, B. Pan, Y. Xie, *J. Am. Chem. Soc.* 140 (2018) 1760–1766.
- [24] G. Marci, E.I. García-López, L. Palmisano, *Eur. J. Inorg. Chem.* 2014 (2014) 21–35.
- [25] H. Lu, J. Gao, Z. Jiang, F. Jing, Y. Yang, G. Wang, C. Li, *J. Catal.* 239 (2006) 369–375.
- [26] X. Jiang, H. Li, W. Zhu, L. He, H. Shu, J. Lu, *Fuel* 88 (2009) 431–436.
- [27] H. Lü, Y. Zhang, Z. Jiang, C. Li, *Green Chem.* 12 (2010) 1954.
- [28] X. He, G. Zhu, J. Yang, H. Chang, Q. Meng, H. Zhao, X. Zhou, S. Yue, Z. Wang, J. Shi, L. Gu, D. Yan, Y. Weng, *Sci. Rep.* 5 (2015) 17076.
- [29] C. Li, Z. Jiang, J. Gao, Y. Yang, S. Wang, F. Tian, F. Sun, X. Sun, P. Ying, C. Han, *Chem. A Eur. J.* 10 (2004) 2277–2280.
- [30] E. Runge, E.K.U. Gross, *Phys. Rev. Lett.* 52 (1984) 997–1000.
- [31] C. Lee, W. Yang, R.G. Parr, *Phys. Rev. B Condens. Matter* 37 (1988) 785–789.
- [32] J. Tomasi, B. Mennucci, R. Cammi, *Chem. Rev.* 105 (2005) 2999–3093.
- [33] M.J. Frisch, et al., *Gaussian 09, Revision D.01*, Gaussian, Inc., Wallingford CT, 2013.
- [34] T. Lu, F. Chen, *J. Comput. Chem.* 33 (2012) 580–592.
- [35] S. Kraner, G. Prampolini, G. Cuniberti, *J. Phys. Chem. C* 121 (2017) 17088–17095.
- [36] X. You, L. Yu, F. Xiao, S. Wu, C. Yang, J. Cheng, *Chem. Eng. J.* 335 (2018) 812–821.
- [37] X. Duan, G. Sun, Z. Sun, J. Li, S. Wang, X. Wang, S. Li, Z. Jiang, *Catal. Commun.* 42 (2013) 125–128.
- [38] B. Zhang, H. Asakura, N. Yan, *Ind. Eng. Chem. Res.* 56 (2017) 3578–3587.
- [39] S. Zhao, Y. Zhang, Y. Zhou, C. Zhang, X. Sheng, J. Fang, M. Zhang, *ACS Sustain. Chem. Eng.* 5 (2017) 1416–1424.
- [40] P. Meng, H. Heng, Y. Sun, J. Huang, J. Yang, X. Liu, *Appl. Catal. B: Environ.* 226 (2018) 487–498.
- [41] X. Kong, S. Wu, L. Liu, S. Li, J. Liu, *Mol. Catal.* 439 (2017) 180–185.
- [42] H. Wang, C. Wang, Y. Yang, M. Zhao, Y. Wang, *Catal. Sci. Technol.* 7 (2017) 405–417.
- [43] J. Thomas, S. Radhika, M. Yoon, *J. Mol. Catal. A: Chem.* 411 (2016) 146–156.
- [44] M. Dvorak, S.H. Wei, Z. Wu, *Phys. Rev. Lett.* 110 (2013) 016402.
- [45] S.A. Mewes, F. Plasser, A. Krylov, A. Dreuw, *J. Chem. Theory Comput.* 14 (2018) 710–725.
- [46] Y. Hu, X. Xu, Y. Jiang, G. Zhang, W. Li, X. Sun, W.Q. Tian, Y. Feng, *Phys. Chem. Chem. Phys.* 20 (2018) 12618–12623.
- [47] Y. Li, C.A. Ullrich, *Chem. Phys.* 391 (2011) 157–163.
- [48] B.R. Moser, R.L. Evangelista, T.A. Isbell, *Energy Fuel* 30 (2016) 473–479.
- [49] H. Lu, J. Gao, Z. Jiang, Y. Yang, B. Song, C. Li, *Chem. Commun.* 2 (2007) 150–152.
- [50] R.V. Mambrini, A.L.M. Saldanha, J.D. Ardisson, M.H. Araujo, F.C.C. Moura, *Appl. Clay Sci.* 83–84 (2013) 286–293.
- [51] Q. Xiang, J. Yu, M. Jaroniec, *J. Am. Chem. Soc.* 134 (2012) 6575–6578.
- [52] X. Zeng, X. Xiao, Y. Li, J. Chen, H. Wang, *Appl. Catal. B: Environ.* 209 (2017) 98–109.
- [53] W. Zhang, H. Zhang, J. Xiao, Z. Zhao, M. Yu, Z. Li, *Green Chem.* 16 (2014) 211–220.
- [54] X.M. Gao, F. Fu, L.P. Zhang, W.H. Li, *Phys. B* 419 (2013) 80–85.
- [55] W.S. Zhu, C. Wang, H.P. Li, P.W. Wu, S.H. Xun, W. Jiang, Z.G. Chen, Z. Zhao, H.M. Li, *Green Chem.* 17 (2015) 2464–2472.
- [56] L. Li, J. Zhang, C. Shen, Y. Wang, G. Luo, *Fuel* 167 (2016) 9–16.
- [57] T. Hirai, Y. Shiraishi, K. Ogawa, I. Komasa, *Ind. Eng. Chem. Res.* 36 (1997) 530–533.
- [58] Y. Shiraishi, Y. Taki, T. Hirai, I. Komasa, *Ind. Eng. Chem. Res.* 38 (1999) 3310–3318.
- [59] J. Bu, G. Loh, C.G. Gwie, S. Dewiyanti, M. Tasrif, A. Borgna, *Chem. Eng. J.* 166 (2011) 207–217.
- [60] M. Styliadi, D.I. Kondarides, X.E. Verykios, *Appl. Catal. B: Environ.* 47 (2004) 189–201.
- [61] V. Brezová, P. Billik, Z. Vrecková, G. Plesch, *J. Mol. Catal. A: Chem.* 327 (2010) 101–109.
- [62] A. Jańczyk, E. Krakowska, G. Stochel, W. Macyk, *J. Am. Chem. Soc.* 128 (2006) 15574–15575.
- [63] Z. Wang, W. Ma, C. Chen, H. Ji, J. Zhao, *Chem. Eng. J.* 170 (2011) 353–362.
- [64] J.H. Shen, J.J. Horng, Y.S. Wang, Y.R. Zeng, *Chemosphere* 182 (2017) 364–372.
- [65] Y. Nosaka, A.Y. Nosaka, *Chem. Rev.* 117 (2017) 11302–11336.
- [66] W. Zhu, B. Dai, P. Wu, Y. Chao, J. Xiong, S. Xun, H. Li, H. Li, *ACS Sustain. Chem. Eng.* 3 (2015) 186–194.
- [67] J.M. Yin, J.P. Wang, Z. Li, D. Li, G. Yang, Y.N. Cui, A.L. Wang, C.P. Li, *Green Chem.* 17 (2015) 4552–4559.
- [68] J.F. Palomeque-Santiago, R. López-Medina, R. Oviedo-Roa, J. Navarrete-Bolaños, R. Mora-Vallejo, J.A. Montoya-de la Fuente, J.M. Martínez-Magadán, *Appl. Catal. B: Environ.* 236 (2018) 323–337.
- [69] H. Tao, T. Nakazato, S. Sato, *Fuel* 88 (2009) 1961–1969.
- [70] E. Baciocchi, M. Bietti, O. Lanzalunga, *Acc. Chem. Res.* 33 (2000) 243–251.